









Multi-method geophysical mapping of ground properties and periglacial geomorphology in Hans Glacier forefield, SW Spitsbergen

Artur Marciniak^{1*} , Marzena Osuch¹ , Tomasz Wawrzyniak¹ ,
Bartosz Owoc¹ , Wojciech Dobiński² , Michał Glazer²
and Mariusz Majdański¹ 

¹ *Institute of Geophysics, Polish Academy of Sciences, Warsaw, 01-452, Poland*

² *Faculty of Natural Sciences, University of Silesia, Sosnowiec, 41-200, Poland*

* *corresponding author <amarciniak@igf.edu.pl>*

Abstract: This article presents the results of a geophysical survey from which detailed images of glacial and periglacial landforms and subsurface structures were obtained. Sediments and landforms on newly deglaciated terrain can be used to reconstruct the extent and character of glaciers in the past and add to the understanding of their response to climate and environmental changes. To derive spatial information from complex geomorphological terrain, joint interpretation of three non-intrusive geophysical methods were applied: Electrical Resistivity Tomography (ERT), Ground Penetrating Radar (GPR), and time-lapse Seismic Tomography. These were used to identify subsurface structures in the forefield of the retreating Hans Glacier in SW Spitsbergen, Svalbard. Three main zones were distinguished and described: outwash plain, terminal moraine from the last glacial maximum, and glacial forefield proximal to the glacier front. Geophysical profiles across these zones reveal information on glacio-fluvial sediment thickness and structure, ice thickness and structure, and bedrock topography. The freezing-thawing effect of the active layer has a strong and deep impact, as demonstrated by variations in P-wave velocity in the obtained outcomes. The results are discussed in the context of the current climate in Svalbard. This study provides a snapshot of ground parameters and the current state of the subsurface in southern Spitsbergen. The boundary between sediment-bedrock layers was estimated to be from 5 to 20 m in depth. It is the first such extensive description of periglacial structures in the forefield of the Hans Glacier, utilising the longest ERT profile (1500 m) in Svalbard together with deep GPR and precise seismic tomography.

Keywords: Arctic, Svalbard, geophysical imaging, periglacial environment, glacial landforms.



Introduction

In recent years, there has been increasing scientific interest in environmental changes within the Arctic and Antarctic regions, as well as in high-altitude landscapes (*e.g.*, Kaushik *et al.* 2021). These areas are highly sensitive to climatic fluctuations and therefore can be used as “natural laboratories” for studying the evolution of periglacial environments, landforms, and processes. In most studies in areas such as Svalbard, the greatest effort is put into the characterisation of air or ground surface temperatures (IPCC 2021). Subsurface parameters and spatial extents of features are usually poorly represented due to an insufficient number of measurements and experiments.

Geophysical imaging is a powerful tool for achieving better spatial insights into subsurface structures. Approaches utilising multiple methods based on different parameters can be effective in recognising structural features and major lithological characteristics, as well as in the indirect estimation of thermal conditions (Maurer and Hauck 2007; Kneisel *et al.* 2008). Freezing of the ground has implications for geomorphic processes, mechanical and hydrogeological properties, and consequently landforms since freezing restricts permeability and subsurface water movement. Materials of different grain sizes have various thermal conductivities and volumetric heat capacities (Zimmerman and King 1986). Most modern permafrost research focuses on the variability of the 0°C isotherm within the ground, known as the permafrost table. Such boundary separates permafrost from the so-called active layer above where seasonal changes in summer reach positive temperatures.

The direct measurement of permafrost, *i.e.*, thermal properties of the ground, can only be done by establishing boreholes equipped with thermistor strings. Such an approach is limited to point observations in a limited number of boreholes and does not provide information about both permafrost/active layer areal changes over time. Instead, multiple geophysical methods can be used in an integrated field investigation to fill this gap. Seasonal changes in both temperature and hydrology of the permafrost/active layer strongly affect the elasticity modulus and, therefore, seismic velocities of rocks (Jacoby *et al.* 1996; Carcione and Seriani 1998). This complicates our understanding of active layer behaviour, which in turn impacts our understanding of the glacial and periglacial environments. As a consequence, integrated seismic studies in permafrost environments remain scarce.

To improve the understanding of landforms–permafrost interactions, joint interpretation of multiple datasets is essential. In this contribution, we present the results of a multi-method geophysical approach utilising Electrical Resistivity Tomography (ERT), Ground Penetrating Radar (GPR) and seismic tomography. These methods were combined to obtain an improved visualisation of subsurface structures of geomorphological landforms in the forefield of the Hans Glacier, including outwash plain (sandur) and terminal moraine.

Study site

The study area is located in SW Spitsbergen near the Polish Polar Station Hornsund (Fig. 1). The station was established in 1957, and since 1978 it has conducted year-round scientific monitoring. Geophysical imaging was conducted in 2015, 2017, and 2018 along with the HOR22 profile in an area partially covered by a glacier up to 2013. The survey was performed on the uplifted marine terraces between the shore of the Hornsund fjord and the slopes of the mountains Fugleberget (569 m a.s.l) and Ariekammen (517 m a.s.l). These terraces, raised during the Holocene (Lindner *et al.* 1986), consist of sea gravels covered by a wide variety of tundra vegetation types as well as areas of exposed rock. The profile also covers the moraines of the Hans Glacier. The glacier retreated about 1500 m from its maximum extent (König *et al.* 2014) at the end of the Little Ice Age (LIA). To image periglacial and glacial features, the profiles were run during two campaigns through moraines towards the terminus of the retreating glacier. There is a slight difference in the profile line obtained on the frontal moraine between the two data acquisition campaigns.

Climatic conditions. — The climate of the west coast of Spitsbergen is highly influenced by relatively mild polar-marine conditions and has experienced significant changes in the annual average air temperature over the 20th century

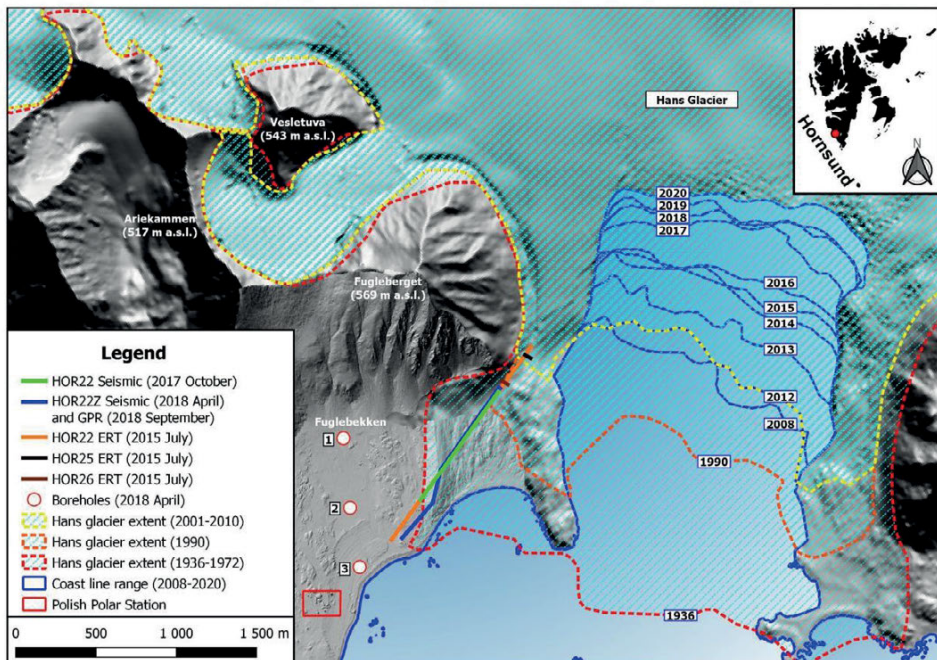


Fig. 1. Study area with marked seismic, ERT, and GPR profiles. Digital elevation model after Błaszczuk *et al.* (2022), glacier extent after König *et al.* (2014).

and after the year 2000 (Nordli *et al.* 2020). Changes in the annual cycles of air temperature during this period are not evenly distributed. Atmospheric warming over Spitsbergen has been pronounced in almost all decades since the end of the LIA, except for the two coldest decades of the 1910s and 1960s. The greatest warming was observed during the past three decades and is amongst the most severe recorded in the Arctic region. The largest impact is seen in the response of glaciers, especially in changes to volume and extent (Van Pelt *et al.* 2019). The location of the front of the Hans Glacier and factors controlling position was described by Błaszczyc *et al.* (2021).

Long-term measurement of meteorological variables at the Hornsund Station enables estimation of changing climatic conditions. Figure 2a shows the variation in mean annual air temperature at Hornsund in the period 1979–2020. The mean air temperature from this period was -3.6°C (and -3.7°C during 1979–2018). Analyses of this data by the modified Mann-Kendall test indicate a statistically significant increasing trend with a slope of $+1.04^{\circ}\text{C}$ per decade, using the method of Sen (1968). This was six times higher than the global warming average for the same period (Wawrzyniak and Osuch 2020). Such changes have many environmental implications, including the prolongation of the ablation season (Osuch and Wawrzyniak 2017b; Nowak *et al.* 2021). Figure 2b shows variation in the number of days with positive air temperature per year observed at Hornsund in the period 1979–2020. The lowest number, 99 days, was observed in 1982, while the highest was 213 days in 2016. A statistically significant increasing trend was estimated with a slope of $+12.86$ days per decade.

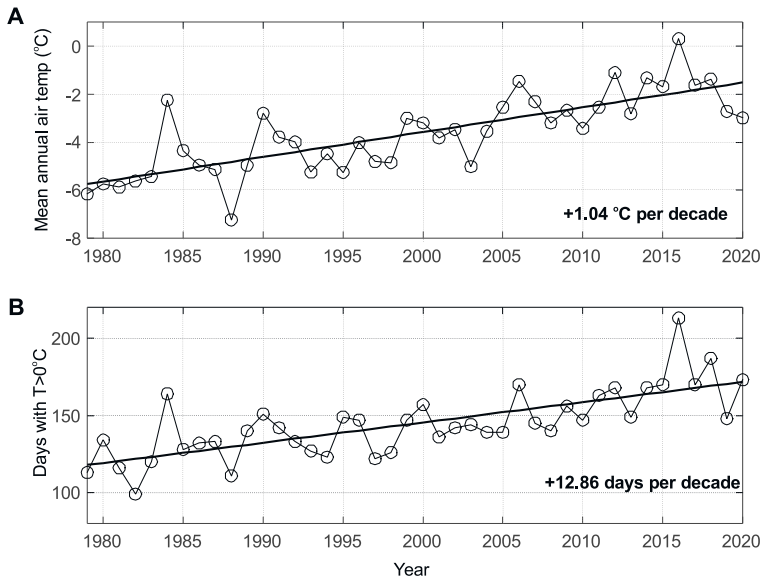


Fig. 2. Variation in (A) annual mean air temperature and (B) number of days with positive air temperatures at Hornsund Station in the years 1979–2020. Trends were estimated by the modified Mann-Kendall test (Hamed and Rao 1998).

Changes in air temperature and precipitation resulted in changes in snow cover thickness and duration (Osuch and Wawrzyniak 2017a). The presence of a seasonal snow cover has a significant influence on the ground thermal regime, with either cooling or warming effects that change over time. Due to high albedo and low thermal conductivity, snow cover acts as an insulator from direct atmospheric influence. Snow cover is a key factor for subsurface processes including both permafrost development and degradation, as it may substantially reduce the seasonal freezing depth. The overall impact of snow cover on the ground thermal regime depends on the timing, duration, thickness, and melting of seasonal snow and ice cover (Wawrzyniak *et al.* 2016; Christiansen *et al.* 2019; 2020, 2021). Figure 3 presents the variation of maximum annual snow depth and the number of days with snow cover at the Hornsund meteorological site in the period 1983–2020. Large decreases in both variables are present with statistically significant trends. The slopes of the trends are -2.35 cm per decade for maximum snow depth and -12.78 days per decade for snow cover duration.

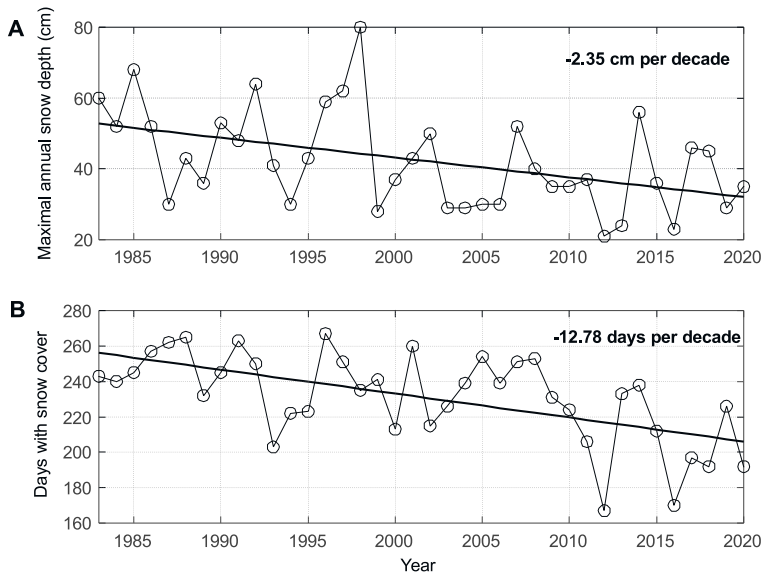


Fig. 3. Variation in (A) maximal annual snow depth and (B) number of days with snow cover at Hornsund Station in the years 1983–2020. Trends were estimated by the modified Mann-Kendall test (Hamed and Rao 1998). The slope of the trend was estimated using Sen’s method (Sen 1968).

Geology and geomorphology of the study site. — The geology along the studied profile (Fig. 4) consists of crystalline Precambrian rocks of Lower and Middle Hecla Hoek succession: marbles, schists, metamorphic quartzites, paragneisses, and amphibolites (Czerny *et al.* 1993). These rocks are strongly fractured and loosened in the near-surface zone due to tectonic relief movements and glacial abrasion and frost weathering at the turn of the Pleistocene/Holocene.

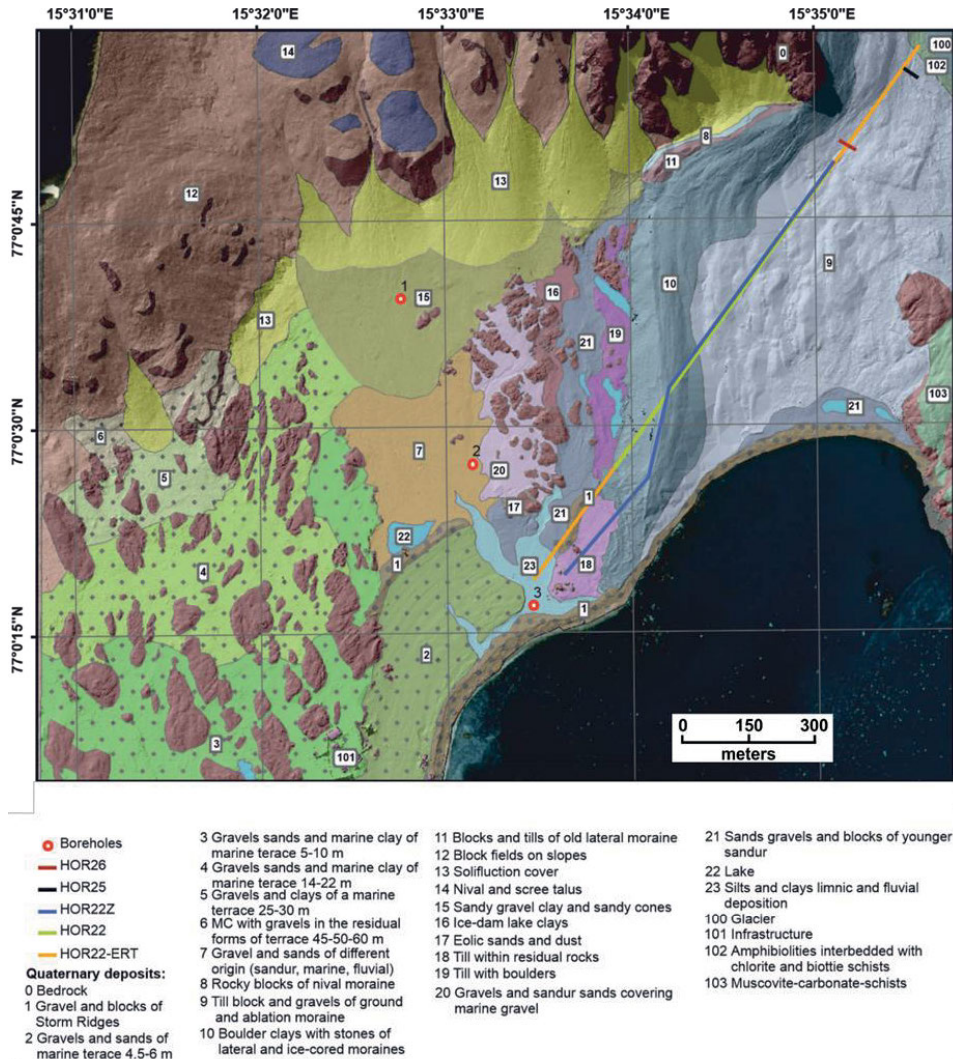


Fig. 4. Map of Quaternary deposits with marked seismic, GPR and ERT lines. Source of data: Pękala (1989) and Glazer *et al.* (2020).

As a result of isostatic uplift, abrasion platforms with variably aged marine sediments were formed. These elevated structures have been largely transformed by erosion, as well as by colluvial accumulation and solifluction on the slopes (Pękala 1989; Dolnicki and Grabiec 2022). Isostatic uplift of terraces on Spitsbergen was irregular and also affected by local tectonic activity (Lindner *et al.* 1986). Uplift depended spatially and dynamically on the distribution of past ice-sheet loads and deglaciation histories (Landvik *et al.* 1998).

In the foreground of the Hans Glacier, landforms of glacial and fluvioglacial relief in the form of moraines, soil and rock deposits were superimposed on the

uplifted sea terraces. These glacial landforms underwent relatively rapid changes in the periglacial environment following deglaciation especially on slopes and in wetlands. The maximum extent of the Hans Glacier is marked by the frontal part of the ice-cored moraine, which was deposited *ca.* 1900 (Fig. 4), at the end of the LIA (Błaszczuk *et al.* 2013). The frontal moraine is characterised by a particularly large culmination of pushed morainic sediments with a buried ice core. Behind this moraine, an area of degrading dead-ice ground moraine extends up to the current glacier front (Glazer *et al.* 2020). Ground moraine deposits formed during advance and retreat also contain blocks of dead ice, visible in the geophysical imaging described below. Within this area, a system of smaller lateral moraines has been created encircling sediments of the ground moraine.

In southern Spitsbergen, there has been a recent expansion of ice-free areas (Fig. 1), with the most remarkable retreats of the tidewater glaciers (Błaszczuk *et al.* 2013, 2021), therefore the monitoring of changes in the functioning of environmental systems has become critically important.

Methods

The ERT measurements were carried out in June 2015, using a Schlumberger and dipole-dipole array with 5 m electrode spacing (Loke 2018). As an electric method, the ERT is sensitive to water saturation and phase changes, as ice has very high resistivity and water has low resistivity. Due to better resolution, only the results from the dipole-dipole arrays are presented in this study. The ERT profile length was 1500 m and covered parts of the Fugglebekken catchment (past glacial outwash plain), along with the Hans Glacier ice-cored moraine of the glacial maximum and post-glacial sediments with dead ice (Fig. 1). The profile ends close to the current glacier front. The dataset was gathered using ABEM Terrameter LS equipment. Additionally, the data from two 40 m crossline profiles (HOR25 and HOR26) were collected at the end of the HOR22 line. These arrays used dense (1 m) electrode spacing for recognition of active layer thickness, with a dipole-dipole scheme.

The GPR survey along 1115 m profile was conducted when the ground was still in a thawing state in September 2018. It covered the HOR22Z profile so that the results from various geophysical methods could have been compared. A MALÅ GPR with a 30 MHz non-shielded RTA (Rough terrain antenna) system was used, allowing penetration up to 40 m. The sampling interval was 20 cm, providing a dense dataset. Elevation was measured by built-in GPS.

Two seismic campaigns were undertaken in September/October 2017 during maximum active layer thawing and in April/May 2018 with the active layer frozen. In September, the seismic receiver and shot spacing was 5 m, and the seismic profile consisted of three deployments with 50 m lateral offsets, resulting in a length of 900 m (without shot offsets) covered with seismic stations, using 4.5 Hz

geophones connected with standalone Omnirecs Data CUBE stations. In April 2018, the profile consisted of four deployments with offset-shooting and 25 m offset on each side, resulting in a length of 1150 m (without shot offsets) covered with seismic stations. The receiver spacing in 2018 was maintained (5 m), whereas the shot spacing was set at 2.5 m. As a result, the data was spatially twice as dense as in 2017. This significantly increased the seismic data fold (Fig. 5) and enhanced the signal-to-noise ratio and horizontal resolution of the data.

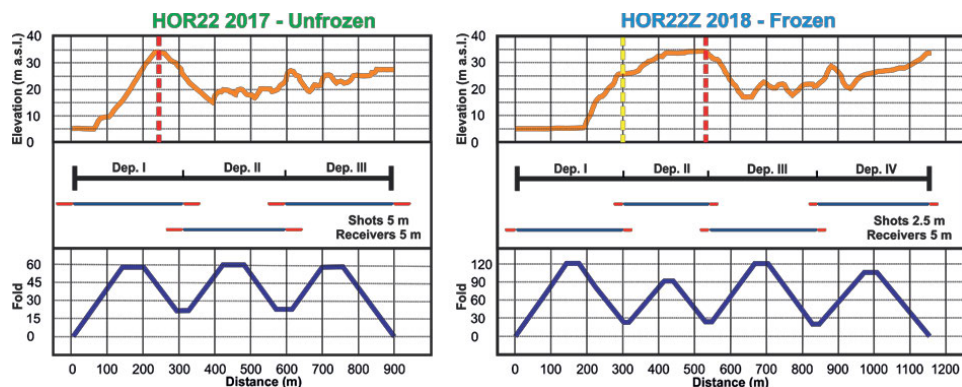


Fig. 5. The survey geometry for seismic profiles during freezing and thawing active layer conditions. The yellow bar crossing the profile marks the edge of the moraine. The red bar marks the beginning of the shared profile in the two seasons, which can be directly compared. Snow coverage during measurements is visible on the elevation profile, however, main landforms can be distinguished and directly compared. Rock outcrops not covered.

Data processing

The program Res2dinv v. 4.06.18 was used to invert the measurement data. For topographic correction, a Digital elevation model (DEM) model with a 1 m resolution was used. More than 50 inversions with respective predetermined parameters were applied to test the behaviour of the resistivity models and to ensure a systematic approach (Glazer *et al.* 2020). Models demonstrated high resilience to structural change upon tested inversion parameters. The resistivity model standard settings from this version of the software for robust data and smooth model were used. The inversion methodology was the same for all three ERT lines.

GPR is one of the most useful tools in cryospheric studies (Farbrot *et al.* 2005; Baelum 2007; Bernard *et al.* 2014; Senderak *et al.* 2021). Data processing was conducted using RadExplorer software. It consists of the removal of instrumental noise (debias), with subsequent basic signal filtering for optimal results. In addition, time zero adjustment was made based on the first breaks of Electromagnetic (EM) waves, with final topography correction based on the GPS data. EM wave velocities were quantified in recognised subsurface structures.

The precise velocity field for depth migration was then determined after manual fitting of parameters, based on tabularized values (Dobiński *et al.* 2011, 2017).

Seismic refraction results were obtained by merging two inversion methods. To image the near-surface layer, the Simultaneous Iterative Reconstruction Technique (SIRT) algorithm (Nolet 2008) was used. Such an approach permits precise estimation of the first seismic boundary, which was fixed for further processing. For modelling of deeper layers, First Arrival Traveltime Tomography (FATT) was applied. This produces a precise estimation of velocity changes and thus gives a smooth velocity field, necessary for recognition of freezing-thawing effects. The starting velocity field model for FATT was a rectangular grid with cell dimensions of 5.0 by 1.0 m in unfrozen conditions (2017) and 2.5 by 1.0 m in frozen conditions (2018). The variation in model cell size is due to different shot spacing for the corresponding survey (Fig. 5). Seismic tomography inversion for both seasons was carried out with the JIVE3D software (Hobro *et al.* 2003). During processing, a set of linearized refinements was applied to the velocity field model for an accurate fit between picked and calculated travel times. For uncertainty analysis, the approach proposed by Owoc *et al.* (2019) was used. It employs a grid search method to statistically generate a set of 1D velocity fields, which are used as starting models in tomographic inversion. To estimate uncertainty, standard deviations of obtained results (inverted velocity fields) were calculated separately for each grid cell.

Results and interpretation

The combined geophysical surveys yielded sufficient data for quantitative and qualitative analysis of the study site. The combination of the different methods allowed resolving the complex characteristics of the subsurface.

Electrical Resistivity Tomography. — The application of ERT with a dipole-dipole array deployment provides insight into the ground structures up to 100 m in depth (Fig. 6). However, due to high resistivity, only the shallowest parts of the image (to a depth of 20–30 m) can be interpreted with certainty. The beginning of the section where the seismic data from profile HOR22Z can be compared with the ERT dataset is located at 520 m of the profile. There is a large variability in resistivity, ranging from 0.1 to 11000 kOhm.m. Such broad variation indicates major changes in conditions for current propagation for different parts of the study site. Multiple bodies of high resistivity can be identified in the profile image. The root mean square error for profile HOR22 was estimated at 5.3%, and 3.7% and 4.5% for profiles HOR26 and HOR25, respectively. The analysis of the ERT results allows for differentiation of 3 zones, where major resistivity distributions can be separated. These zones correspond to the geomorphological overall zonation/landforms: outwash plain (sandur), terminal moraine, and ground moraine (glacier forefield).

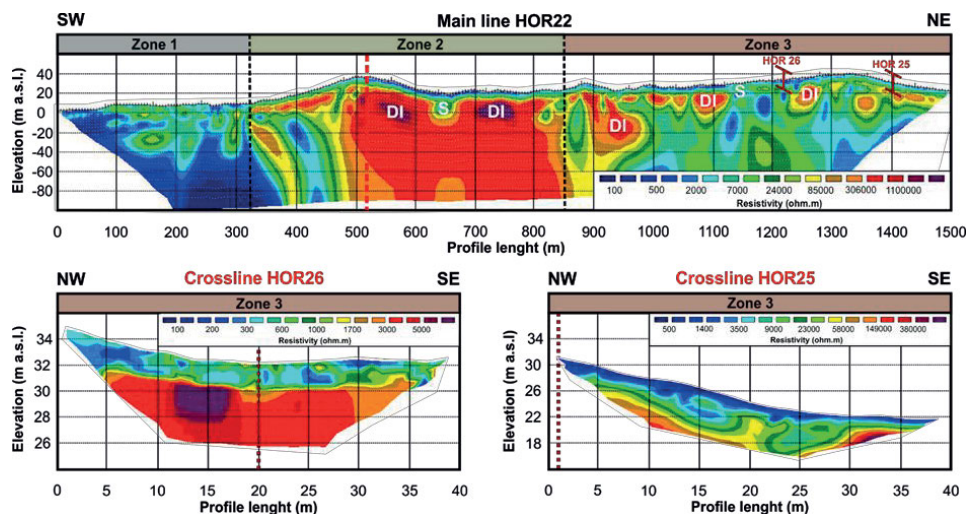


Fig. 6. Profiles generated by ERT survey (summer 2015) using dipole-dipole electrode deployment. High-resistivity anomalies were interpreted as dead-ice (DI). The small low-resistivity anomalies at 640 and 1150 m were identified as an active watercourse (S). The red dashed line indicates the area from which the results of seismic and GPR surveys can be directly compared. The crossline profiles HOR25 and HOR26 show the presence of the active layer with thickness varying from 1 to 2 m. Profiles differ in scale concerning both elevation and resistivity. For the location of the profiles, see Fig. 1.

In zone 1 (outwash plain), from 0 to 320 m on the profile, overall resistivities are low, in the range of 0.1 to 7.0 kOhm.m. This can be attributed to the presence of the water-saturated layers in the Fuglebekken catchment. The lowest resistivity occurs between 0 and 80 m due to the presence of water-saturated sands and gravels of the Fuglebekken channel and floodplain. Increasing resistivity from 80 to 240 m can be attributed to a thin cover of silts, sands, and gravels of the outwash plain, formed as a sandur in the past, by meltwater from the glacier (Glazer *et al.* 2020). Structures located at 150–170 m and 300–320 m can be identified as gravel and blocks of storm ridges, which are visible on the surface as outcrops (Fig. 4).

In zone 2 (terminal moraine), from 320 to 850 m along with the profile, the terminal moraine of the maximum glacial extent during the LIA at around 1900 has the highest resistivity (over 1100 kOhm.m). The structure can be interpreted as dead-ice. On the SW side of the moraine, the ice core is thinner compared to the NE side. Near the surface above these ice cores, a water-saturated sediment cover that is around 10 m thick can be noticed based on estimated resistivity values. In addition, on the NE side of the moraine at 640 m, a stream channel is visible by clearly lower resistivity values. In the profile between 320 up to 850 m, features at a depth greater than 20 m below the surface cannot be identified, as the current is blocked by overlying high-resistivity features. Thus, the interpretation of deeper parts is uncertain and may be misleading.

In zone 3 (glacier forefield proximal to the glacier front), from 850 m to 1500 m, several structures are present with differing resistivities. Multiple areas with lower resistivity (<30 kOhm.m) can be interpreted as a water-saturated layer and stream channels due to the overall shape of the anomalies. Structures with high resistivity (>100 kOhm.m) can be recognised as blocks of dead-ice 10–30 m big. From 1280 m to 1500 m, structures with moderate resistivities can be seen. These are probably solid rock structures, with relatively high values of resistivity, however significantly lower than typical ice formations. Additionally, the shape of the structures is more horizontal in comparison to dead ice blocks. Within the zone 3, periglacial reworking of glaciogenic sediments occurred during ongoing deglaciation. The retreat of the Hans Glacier caused progressive modification of glacial sediments, landforms, and deeper layers through exposure to non-glacial processes, resulting in complex structures.

Crossline profiles gathered in June 2015, HOR25 and HOR26 were used to image the active layer thickness in Zone 3 with denser electrode spacing on 40 m arrays. The difference to mainline HOR22 deployment resulted in shallower recognition depth, however, with higher resolution. The layer varies from 1 to 2.5 m in both crossline profiles. There is an overall difference in resistivity between HOR26 (approx. 5.0 kOhm.m) and HOR25 (380 kOhm.m). This can be explained by the localisation of the profile HOR26 near the active surface stream, while line HOR25 was located on a relatively dry part of the moraine. The increased resolution due to more dense electrode spacing allowed for recognition of active layer – permafrost boundary, which is clearly visible on HOR26 line at a depth of average 2 m. Such boundary is less visible at line HOR25 due to lower contrast between layers in a drier environment. In comparison to profile HOR22, where the active layer is not visible due to resolution limitations, the shorter lines HOR25 and HOR26, in contrast, do not show the sediment-bedrock boundary.

Ground Penetrating Radar. — Due to resolution limitations, the GPR method with a 30 Mhz unshielded RTA provides information about subsurface structures down to 40 m depth but not the near-surface, including the active layer (Fig. 7). The shallowest penetration range was obtained at the end and beginning of the profile and at 100 m of its length, where it reached 20 m. The deepest penetration was in the central part of the terminal moraine. The overall reflection visibility is good, and multiple reflectors can be tracked and distinguished as continuous across the whole profile. Reflections at depths greater than 10 m in front of and behind moraine structures are very irregular. In the dataset, almost no diffraction hyperbolas can be distinguished. These observations indicate that irregular structures are continuous, without visible faults and discontinuities. Similar to the ERT results, the three main zones could be distinguished.

Zone 1 (the outwash plain) ranges from 0 to 220 m of the profile, with shallow sediment cover visible on the GPR section. The thickness of this layer, limited by the green dashed line (Fig. 7), varies from 1 m at the beginning of the profile to about 7 m near the slope of the terminal moraine. Beneath this layer,

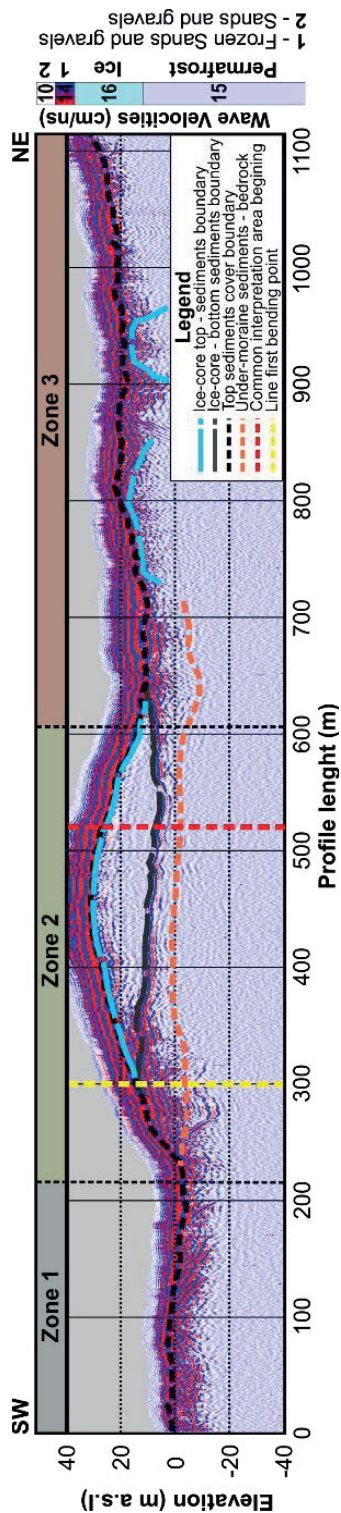


Fig. 7. The GPR images reveal a sediment layer covering the moraine structure and uniform LIA moraine with an ice core inside. The red and yellow dashed lines indicate the profile breaking points.

crystalline bedrock can be distinguished. The uneven shape of this boundary is caused by the presence of gravel and blocks of storm ridges partly covered by sediments (Fig. 4).

Zone 2 (terminal moraine) from 220 to 620 m of the profile length includes the terminal moraine from the maximum glacial extent during the LIA. The ice core was recognised in the processed radargram by its shape from 300 up to 610 m of the profile, beneath 5 to 7 metres of sediment cover. Presumably, a body of glacial ice was buried at the glacier terminus by accumulations of sediment during the glacier recession (Evans 2009). These overlying sediments provide a protective layer that reduces or even prevents the melting of the ice core as the active layer thickness is much smaller than the sediment cover. As the signal in this layer (up to an average of 35 m under the surface) reveals no reflective characteristics, the ice-core can be described as uniform without internal structures. Underneath the ice-core, there is a boundary that strongly reflects EM waves (dark grey dashed line on Fig. 7) that separates it from underlying sediments. The thickness of this lower sediment layer varies from 20 m in the bottom of the terminal moraine to 6 m in its NE slope (540 m of profile length). The shape of the layer at 230–330 m is a result of sediments pushed during glacial advance and debris sliding down from the slopes of the terminal moraine itself. The signal in this layer is strongly dampened, with most energy from the EM wave being propagated to the surface. The use of GPR also allowed for the distinction of the sediment/bedrock boundary and the bedrock layer (orange line on Fig. 7). The elevation of

this boundary is located at around 1 m a.s.l. A uniform ice-core partially isolates the underlying sediments and bedrock from hydrological processes occurring at the surface.

Zone 3 (the glacial forefield proximal to the glacier front), located from 610 m to the end of the profile, is covered by glacial deposits 5–10 m thick. Below this layer, the change in signal characteristics was identified as dead ice blocks mixed with englacial debris. Due to complicated reflections patterns, the interpretation of deeper structures reveals complex transitions. They have very high resistivity and effectively reflect EM waves to the surface. Deeper layers are obscured by these structures and by water saturation of near-surface sediment, which absorbs EM wave energy. As a result, only the tops of the dead-ice blocks can be imaged using the GPR method. Within zone 3, there are various glacio-fluvial landforms, characteristic of young glacial landscapes in a ground moraine. These landforms were formed below and around the margins of the retreating glacier and include old meltwater channels, eskers, and kame terraces, as can be recognised from the irregular topography of this zone and the shape of the sediment-bedrock boundary.

Seismic Tomography. — Seismic tomography imaging was conducted during two seasons, with maximal freezing (April 2018) and thawing conditions (October 2017). The application of seismic tomography was focused on the recognition of lithological structures and the top of permafrost. The tomographic results were obtained with the joint application of two methods. The shallowest layer was identified with short offset refraction travel times and the SIRT algorithm. The deeper layer was imaged using the ray-based FATT approach (Hobro and Singh 1999) with a fixed layer from the SIRT approach (Nolet 2008). Such a combination allowed for the improvement of subsurface recognition, with the derivation of sharp boundaries as well as smooth velocity changes. The initial models for tomographic method inversion were based on the GPR and ERT results. In these models, two layers were approximated: sediment and bedrock. The maximum penetration of imaging reached 80 m under the terminal moraine surface. The method provides a deeper range than GPR, but due to high seismic velocities and resolution limitations, smaller structures such as dead-ice blocks visible on the ERT and GPR in the glacial forefield cannot be recognised. The most important added value from the use of the SRT method is the visibility of seasonal changes in seismic velocity, *i.e.*, the thawing-freezing effect. During the field campaign in October 2017, air temperatures were still above 0°C, and the active layer thickness was estimated to be about 2 m, based on the data from nearest boreholes in Fuglebekken catchment (Fig. 1), while in April 2018, the air temperatures remained below 0°C and the ground was frozen.

Zone 1 (the outwash plain) from 280 to 390 m of the 2017 profile and 0 to 220 m of the 2018 profile, is characterised by uniform velocities across the sediment cover (~2000 m/s and 2500–2700 m/s in consecutive years). This is the smallest seasonal velocity change observed for the sedimentary cover along the

whole profile. A slight mismatch at the 5 m depth is a result of differing profile locations. In the bedrock, differences in the velocity field are visible up to 20 metres under the surface. In the data from 2017, velocities at 10 m depth below the surface are close to 5000 m/s, while for 2018, they were estimated at around 5600 m/s. Such high velocities indicate that the basement was in a cryotic state in April 2018 and September 2017, and the relatively small changes in the velocity compared to the other parts of the study site are probably related to groundwater level changes induced by the freezing-thawing effect of the active layer. However, the effect of velocity change is visible up to even 30 m under the surface. The changes in hydrology can reach even deeper into the rock structures and thus require further studies.

Zone 2 (terminal moraine), from 220 m in 2017 and 400 m in 2018 to 600 m, is characterised by clearly visible changes in velocity in sediment cover (2000 and 3000 m/s) and underlying ice-core (4000 and 5000 m/s in subsequent seasons). Due to the nature of refracted waves, the boundary between the ice-core and underlying structure cannot be recognised. The debris layer, visible in the GPR image underlies the ice-core, has lower velocities thus is transparent for refracted waves. Moreover, due to a mixture of ice and rocks lying on water-filled bedrock, there is no clear velocity change that could be observed in refracted waves. Because of this complicated pattern, the maximum refraction penetration is limited to the depth of 20 m only, as shown in Fig. 8. The uncertainty analysis for the second, deeper layer reveals very good precision, with an average value of ± 50 m/s for the first 20 m and ± 150 m/s in deeper areas in 2017, and not exceeding ± 200 m/s for deeper parts of the 2018 profile.

Zone 3 (the glacier forefield proximal to the glacier front) from moraine to the current glacier shows a simple velocity structure with clear ~ 7 m thick sediment over bedrock. Comparison of results from two seasons shows the change of velocity down to 37 m. The uncertainty in both cases is smaller than the overall velocity change. Below these depth velocities are unaffected by seasons. Velocity changes in the sediment layer reach 2000 m/s, whereas, in bedrock, they exceed 1000 m/s. These differences in the velocity field between the two seasons are due to changes in the state of water/ice. The effects of such changes are visible almost up to 40 m under the surface (see deepest area on Fig. 9), however a more precise estimation of hydrological changes require direct studies and cannot be estimated with higher certainty using currently gathered geophysical data. In September 2017, velocities in the upper sediment layer were around 2000 m/s, corresponding to water-saturated sand, whereas velocities of 4000 m/s in April 2018 correspond to the same mixture in a frozen state. The bedrock in the unfrozen season is characterised by velocities around 4000 m/s, representing fractured due to thaw/freeze cycles and water-filled bedrock. In April 2018, bedrock velocities were significantly larger (6300 m/s) as water between grains was completely frozen. The uncertainty results for that layer are similar to those in zone 1, with an average of ± 100 m/s for the first 20 m. Below

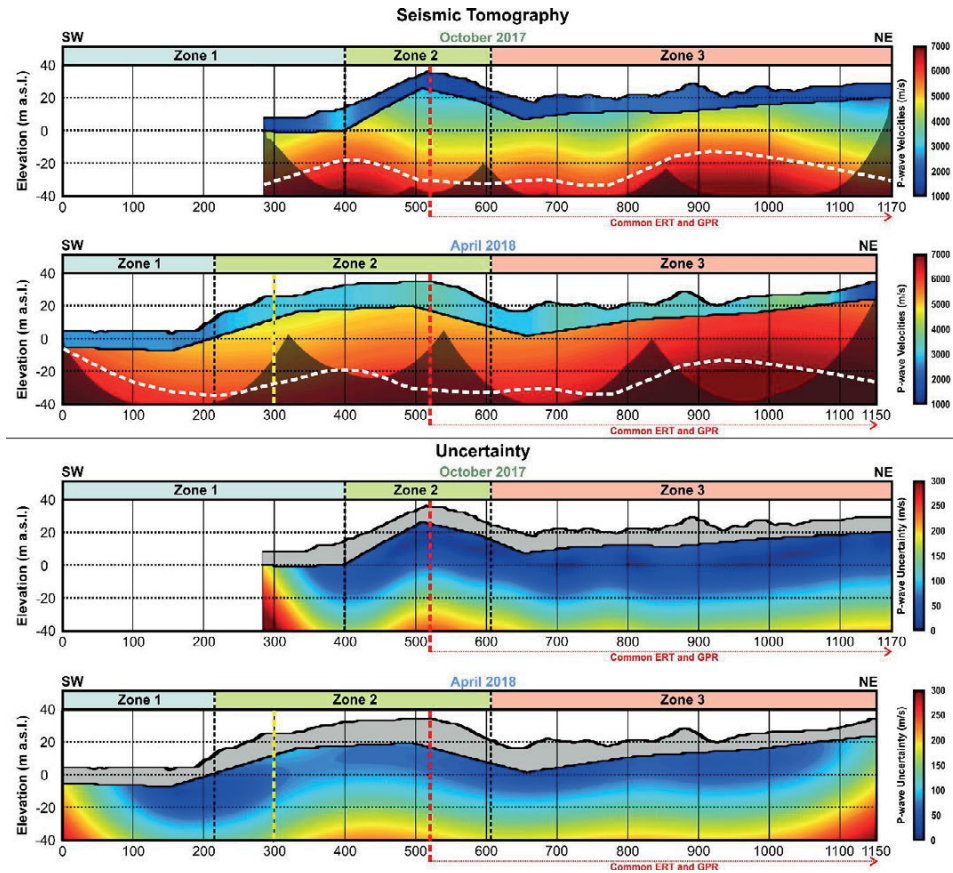


Fig. 8. Results of the Seismic Tomography analysis. The white dashed line marks the boundary of seasonal velocity changes. The uncertainty of the estimated velocity field is small, on average less than 100 m/s. The red and yellow dashed lines indicate the breaking points of the seismic profile. The red line additionally indicates the same location of ERT and GPR profile following NE direction. The grey-shaded masks show the ray propagation depth on tomographic images. Due to the used inversion algorithms for deeper layers imaging, the uncertainty analysis was possible for those layers where ray coverage was precisely estimated.

a depth of 37 m, the uncertainty of the method increases significantly, and thus the seasonal variation of velocity cannot be confirmed.

Integrative approach. — Geophysical remote sensing methods such as GPR, ERT, and active seismic have been used in permafrost research in a few locations in Svalbard to map subsurface structures and composition (Brandt *et al.* 2007; Kasprzak *et al.* 2017; Glazer *et al.* 2020). Although accurate knowledge of active layer thickness distribution and bedrock topography is essential to understand the long-term dynamics of permafrost, data with a time-lapse approach so far were lacking in the forefield of the Hans Glacier and generally in non-glaciated areas of SW Spitsbergen.

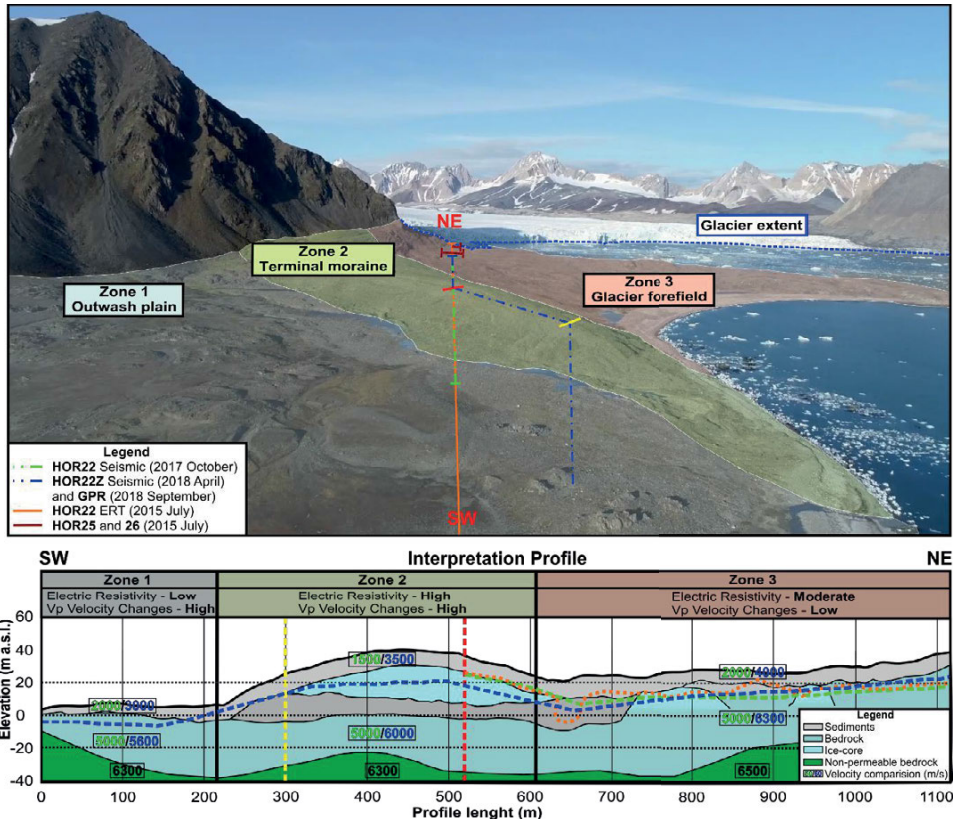


Fig. 9. Interpretation profile from combined methodologies. Several geological structures are present in the study site, with multiple cryotic effects affecting the overall sediment state.

Seismic methods were also used in Svalbard, mainly in the Adventdalen and in waters surrounding the archipelago. The primary purpose of using seismic soundings was to image the deep structures with wide-angle refraction methods (Czuba *et al.* 2008) or reflection seismic imaging (Baelum *et al.* 2012), and both proved successful. In near-surface application, seismic was used to study Pingo structures (Rossi *et al.* 2017; Hammock *et al.* 2021), clearly showing complicated shallow structures.

A key aspect of this study is that the various geophysical methods are complementary, with each method providing additional information on particular characteristics of the subsurface morphology and morphometric features. Similarly to the work of Hammock *et al.* (2021), where ERT and refraction tomography was used to study incipient coastal open-system Pingo in Svalbard, the use of multiple geophysical methods to study the periglacial environment increases the overall quality of final data and solves interpretation misambiguities.

The application of a comprehensive non-intrusive geophysical approach to studying the moraines and forefield of the Hans Glacier reveals the complex glacial and periglacial nature of the study site. From these results, an interpretation profile was created (Fig. 9) and applied to the study area. For correct interpretation of the data, the sensitivities, resolution, limitations, and uncertainties of different geophysical methods have to be fully considered. Each geophysical method is sensitive to different physical parameters, limiting the ability to accurately describe the subsurface periglacial structures (Table 1). In particular, the effects of seasonal freezing-thawing cycles, which can vary from year to year, must be taken into account, and this requires a multi-method approach. As presented, applied geophysical methods resulted in the slightly different mapping of the same structures, which complement and enable an overall interpretation supported by the geomorphological mapping.

Table 1.

A summary of the obtained results. Advantages (+) and disadvantages (-) of using different geophysical methods to recognise underground structures.

Recognised structure	ERT	GPR	Seismic tomography
The active layer (freezing-thawing effect)	+	-	+
	visible on profiles HOR25 and HOR26 with dense electrode array	due to 30 Mhz antenna with low resolution and measurement in one season only	visible as a VP (P-wave velocity) difference in two seasons both for sediment cover and bedrock
Moraine's ice-core	+	+	-
			not sufficient spatial resolution
Sediment-bedrock boundary	-	+	+
	due to the high water saturation and complicated geology the boundaries are smoothened		
Boundary between ice-core of moraine and underlying sediment	-	+	-
	due to high resistivity values of upper laying ice-core		lack of refraction in low-velocity layers

The ERT method allowed for recognition of active layer thickness, and the presence of ice cores. The general recognition of the study site across profile HOR22, however, without detailed recognition due to limited resolution of wide electrode spacing. Similar to the work of Kasprzak (2015), the results indicate the active layer thickness by using denser arrays in profiles HOR25 and HOR26. Even though resistivity images are smoothed models of near-surface

data, the overall information is sufficient for the recognition of geomorphological features in the study site without the knowledge of precise boundaries of periglacial structures (Glazer *et al.* 2020). However, the results of the ERT method have to be taken with caution in situations where saline water infiltration can happen and thus act as a conductor (Revil and Glover 1998). Multiple ERT profiles with dense electrode deployment are required to obtain more information about active-layer horizontal changes across the study site. Even though, for obtaining a more detailed image of the subsurface, the integration of both data from dense as well as wider arrays providing deeper insight into the subsurface is necessary.

The GPR with a 30 Mhz antenna allowed for detailed recognition of the shapes of the boundaries between uppermost sediments, bedrock, and ice cores. Similarly as described by Brandt *et al.* (2007), the sediment layering can be recognised and tracked. However, due to the resolution limitations of low-frequency RTA, more detailed recognition of the first two metres is not possible, including the active layer. For such a study, a more resolved antenna of 200 Mhz and above will be more suitable. The sediment-bedrock boundary underneath the ice core of the terminal moraine was mapped this way, which was not possible using other geophysical methods. The potential use of antennas with higher frequencies (100 Mhz and higher) in the imaging of the active layer is high, but at the cost of depth resolution and the visualisation of moraine structures (Sevestre *et al.* 2015; Zhao *et al.* 2016). In addition, the scattering of GPR waves by loose rock, unconsolidated sediment and water in a partially or fully frozen state further limits the imaging potential.

The seismic method provided insight into seasonal changes by visualising stages between thawing and freezing based on the velocity change. Based on a direct comparison of velocity fields gathered in the contrasting thermal conditions, and including the uncertainty estimation, this effect can be quantified. It was estimated that the effects of water penetration into the permafrost can be confirmed down to a depth of 40 m. However, due to a lack of information about the bedrock from the deep boreholes, the deepest borehole near the study site reaches 20 m only, future efforts in this subject should be taken. Hilbich (2010) suggested that refraction is very shallow due to high-velocity contrast at the permafrost table. In contrast, this study suggests that deeper penetration is feasible. In unfrozen materials, when the contrast should be greatest, water penetration smooths the velocity gradient resulting in a gradual increase of seismic velocity with depth. Although the acquisition of seismic data requires more effort and is more time-consuming than other geophysical methods, seismic imaging gives a reliable geophysical characterization of deep structures with quantitative uncertainties. This, combined with precise repeatability in the form of time-lapse images, allows recognition of P-waves velocity changes at depths up to 40 m. Such deep seasonal changes can be attributed to hydrogeological processes like deep water percolation. To verify this interpretation, direct

measurements in deep enough cored boreholes (geological structure), thermal measurements (seasonal temperature change), and hydrogeological piezometers (groundwater flow) are necessary.

Concluding remarks

The goal of the geophysical investigations conducted across multiple landforms from sandur, over a terminal moraine up to the present front of the Hans Glacier was to provide comprehensive information on near-surface structural features and characteristics of the periglacial environment. The results presented here highlight the value of combining geophysical techniques for assessing permafrost characteristics, the extent of bedrock and sediment cover, recognition of active layer behaviour, and resolving complex geological structures. The observed freezing-thawing effects are stronger than expected from previous studies due to an indirect influence on deeper structures reaching about 40 m below the surface as a result of deep water penetration into the rock structures. The new geophysical data from three main zones: outwash plain, terminal moraine, and ground moraine in the glacial forefield strongly vary in measured physical properties. Each zone is characterised by a different response to the freezing and thawing effect. Based on two season observations, thermal and hydrogeological effects on geophysical data can be distinguished from the non-seasonal effects of sedimentary thickness and bedrock topography. The main cause of seasonal variation is deep water circulation and intra permafrost percolation in bedrock.

Recently, snow cover, temperature and precipitation are changing rapidly in the Arctic, especially in Spitsbergen. To estimate the influence of these changes on the shift in the periglacial processes, the ongoing time-lapse characterisation of permafrost is required. As there is a clear need to recognise subsurface changes caused by climate warming, geoelectric, seismic, and GPR measurements should be conducted and repeated along with the common profiles, especially in places important for local communities and vulnerable to geophysical hazards. As shown here, such combinations of geophysical methods are effective tools even in places with complex geomorphology. Geophysical methods are non-invasive and provide 2D or 3D images of subsurface features that relate to the interplay of permafrost, water, and ice in the ground and form an excellent basis for comparative studies.

Acknowledgements. — This research was funded by National Science Centre, Poland Grant UMO-2015/21/B/ST10/02509. Part of this work was supported within statutory activities No. 3841/E-41/S/2018 of the Ministry of Science and Higher Education of Poland. Authors want to thank Daniel Dunkley for the language corrections, which significantly improved the quality of the article. Special thanks to the reviewers who have made important suggestions and contributions to this article.

References

- Baelum K. 2007. Investigations of the subsurface by Ground Penetrating Radar (GPR); Examples from Spitsbergen. *AGU Fall Meeting Abstracts 2007*: NS14A-07.
- Baelum K., Johansen T.A., Johnsen H., Rod K., Ruud B.O. and Braathen A. 2012. Subsurface structures of the Longyearbyen CO₂ Lab study area in Central Spitsbergen (Arctic Norway), as mapped by reflection seismic data. *Norwegian Journal of Geology* 92: 377–389.
- Bernard E., Friedt J.M., Sainetony A., Tolle F., Griselin M. and Marlin C. 2014. Where does a glacier end? GPR measurements to identify the limits between valley slopes and actual glacier body. Application to the Austre Lovénbreen, Spitsbergen. *International Journal of Applied Earth Observation and Geoinformation* 27: 100–108. doi: [10.1016/j.jag.2013.07.006](https://doi.org/10.1016/j.jag.2013.07.006)
- Błaszczczyk M., Jania J. A. and Kolondra L. 2013. Fluctuations of tidewater glaciers in Hornsund fjord (southern Svalbard) since the beginning of the 20th century. *Polish Polar Research* 34: 327–352. doi: [10.2478/popore-2013-0024](https://doi.org/10.2478/popore-2013-0024)
- Błaszczczyk M., Jania J., Ciepły M., Grabiec M., Ignatiuk D., Kolondra L., Kruss A., Luks B., Moskalik M., Pastusiak T., Strzelewicz A., Walczowski W. and Wawrzyniak T. 2021. Factors controlling terminus position of Hansbreen, a tidewater glacier in Svalbard. *Journal of Geophysical Research: Earth Surface* 126: e2020JF005763. doi: [10.1029/2020JF005763](https://doi.org/10.1029/2020JF005763)
- Błaszczczyk M., Laska M., Sivertsen A. and Jawak S.D. 2022. Combined use of aerial photogrammetry and terrestrial laser scanning for detecting geomorphological changes in Hornsund, Svalbard. *Remote Sensing* 14: 601. doi: [10.3390/rs14030601](https://doi.org/10.3390/rs14030601)
- Brandt O., Langley K., Kohler J. and Hamran S.E. 2007. Detection of buried ice and sediment layers in permafrost using multi-frequency Ground Penetrating Radar: A case examination on Svalbard. *Remote Sensing of Environment* 111: 212–227. doi: [10.1016/j.rse.2007.03.025](https://doi.org/10.1016/j.rse.2007.03.025)
- Carcione J.M. and Seriani G. 1998. Seismic and ultrasonic velocities in permafrost. *Geophysical Prospecting* 46: 441–454. doi: [10.1046/j.1365-2478.1998.1000333.x](https://doi.org/10.1046/j.1365-2478.1998.1000333.x)
- Christiansen H.H., Gilbert G.L., Demidov N., Guglielmin M., Isaksen K., Osuch M. and Boike J. 2019. Permafrost thermal snapshot and active-layer thickness in Svalbard 2016–2017. In: Orr E., Hansen G., Lappalainen H., Hübner C. and Lihavainen, H. (eds.) *SESS report 2018*. Svalbard Integrated Arctic Earth Observing System, Longyearbyen: 26–47.
- Christiansen H.H., Gilbert G.L., Demidov N., Guglielmin M., Isaksen K., Osuch M. and Boike J. 2020. Permafrost temperatures and active layer thickness in Svalbard during 2017/2018. In: Van den Heuvel F., Hübner C., Błaszczczyk M., Heimann M. and Lihavainen H. (eds.) *SESS report 2019*. Svalbard Integrated Arctic Earth Observing System, Longyearbyen: 236–249.
- Christiansen H.H., Gilbert G.L., Demidov N., Guglielmin M., Isaksen K., Osuch M. and Boike J. 2021. Ground ice content, drilling methods and equipment and permafrost dynamics in Svalbard 2016–2019 (PermaSval). In: Moreno-Ibáñez M., Hagen J.O., Hübner C., Lihavainen H. and Zaborska A. (eds.) *SESS report 2020*. Svalbard Integrated Arctic Earth Observing System, Longyearbyen: 258–275. doi: [10.5281/zenodo.4294095](https://doi.org/10.5281/zenodo.4294095)
- Czerny J., Kieres A., Manecki M. and Rajchel J. 1993. *Geological map of the SW part of Wedel Jarlsberg Land Spitsbergen, 1:25 000*. Institute of Geology and Mineral Deposits. University of Mining and Metallurgy, Cracow.
- Czuba W., Grad M., Guterch A., Majdański M., Malinowski M., Mjelde R., Moskalik M., Środa P., Wilde-Piórko M. and Nishimura Y. 2008. Seismic crustal structure along the deep transect Horsted’05, Svalbard. *Polish Polar Research* 29: 279–290.
- Dobiński W., Grabiec M. and Gądek B. 2011. Spatial relationship in interaction between glacier and permafrost in different mountainous environments of high and mid-latitudes, based on GPR research. *Geological Quarterly* 55: 375–388.
- Dobiński W., Grabiec M. and Glazer M. 2017. Cold–temperate transition surface and permafrost base (CTS–PB) as an environmental axis in glacier–permafrost relationship, based on research

- carried out on the Storglaciären and its forefield, northern Sweden. *Quaternary Research* 88: 551–569. doi: 10.1017/qua.2017.65
- Dolnicki P. and Grabiec M. 2022. The thickness of talus deposits in the periglacial area of SW Spitsbergen (Fugleberget Mountainside) in the light of slope development theories. *Land* 11: 209. doi: 10.3390/land11020209
- Evans D.J.A. 2009. Controlled moraines: origins, characteristics and paleoglaciological implications. *Quaternary Science Reviews* 28: 183–208. doi: 10.1016/j.quascirev.2008.10.024
- Farbrot H., Isaksen K., Eiken T., Kääb A. and Sollid J.L. 2005. Composition and internal structures of a rock glacier on the strandflat of western Spitsbergen, Svalbard. *Norsk Geografisk Tidsskrift-Norwegian Journal of Geography* 59: 139–148. doi: 10.1080/00291950510020619
- Glazer M., Dobiński W., Marciniak A., Majdański M. and Błaszczuk M. 2020. Spatial distribution and controls of permafrost development in non-glacial Arctic catchment over the Holocene, Fuglebekken, SW Spitsbergen. *Geomorphology* 358: 107128. doi: 10.1016/j.geomorph.2020.107128
- Hamed K.H. and Rao A.R. 1998. A modified Mann-Kendall trend test for autocorrelated data. *Journal of Hydrology* 204: 182–196. doi: 10.1016/S0022-1694(97)00125-X
- Hammock C.P., Kulesa B., Hiemstra J.F., Hodson A.J. and Hubbard A. 2021. Seismic and electrical geophysical characterization of an incipient coastal open-system Pingo: Lagoon Pingo, Svalbard. *Earth and Space Science* 9: e2021EA002093. doi: 10.1029/2021EA002093
- Hilbich C. 2010. Time-lapse refraction seismic tomography for the detection of ground ice degradation. *The Cryosphere* 4: 243–259. doi: 10.5194/tc-4-243-2010
- Hobro J.W. and Singh S. 1999. Joint interface and velocity estimation in three dimensions (JIVE3D). *LITHOS science report*. Department of Earth Sciences, University of Cambridge, Cambridge.
- Hobro J.W.D., Singh S.C. and Minshull T.A. 2003. Three-dimensional tomographic inversion of combined reflection and refraction seismic traveltime data. *Geophysical Journal International* 152: 79–93. doi: 10.1046/j.1365-246X.2003.01822.x
- IPCC 2021. *Climate Change 2021: The physical science basis. Contribution of working group I to the sixth assessment report of the Intergovernmental Panel on Climate Change*. Cambridge University Press, Cambridge.
- Jacoby M., Dvorkin J. and Liu X. 1996. Elasticity of partially saturated frozen sand. *Geophysics* 61: 288–293. doi: 10.1190/1.1443951
- Kasprzak M. 2015. High-resolution electrical resistivity tomography applied to patterned ground, Wedel Jarlsberg Land, south-west Spitsbergen. *Polar Research* 34: 25678. doi: 10.3402/polar.v34.25678
- Kasprzak M., Strzelecki M.C., Traczyk A., Kondracka M., Lim M. and Migala K. 2017. On the potential for a bottom active layer below coastal permafrost: the impact of seawater on permafrost degradation imaged by electrical resistivity tomography (Hornsund, SW Spitsbergen). *Geomorphology* 293: 347–359. doi: 10.1016/j.geomorph.2016.06.013
- Kaushik H., Ramanathan A.L., Soheb M., Shamurailatpam M.S., Biswal K., Mandal A. and Singh C. 2021. Climate change-induced high-altitude lake: Hydrochemistry and area changes of a moraine-dammed lake in Leh-Ladakh. *Acta Geophysica* 69: 2377–2391. doi: 10.1007/s11600-021-00670-x
- Kneisel C., Hauck C., Fortier R. and Moorman B. 2008. Advances in geophysical methods for permafrost investigations. *Permafrost and Periglacial Processes* 19: 157–178. doi: 10.1002/ppp.616
- König M., Nuth C., Kohler J., Moholdt G. and Pettersen R. 2014. A digital glacier database for Svalbard. In: Kargel J.S., Leonard G.J., Bishop M.P., Kaab A. and Raup B. (eds.) *Global land ice measurements from space*. Springer, Berlin, Heidelberg: 229–239.
- Landvik J.Y., Bondevik S., Elverhi A., Fjeldskaar W., Mangerud J., Siegert M.J., Salvigsen O., Svendsen J. and Vorren T.O. 1998. The Last Glacial Maximum of Svalbard and the Barents

- Sea area: ice sheet extent and configuration. *Quaternary Science Reviews* 17: 43–75. doi: 10.1016/S0277-3791(97)00066-8
- Lindner L., Marks L. and Pękala K. 1986. Outline of Quaternary chronostratigraphy of the northern Hornsund area, southern Spitsbergen. *Bulletin of the Polish Academy of Sciences. Earth Sciences* 34: 427–436.
- Loke M.H. 2018. *Tutorial: 2-D and 3-D electrical imaging surveys*. URL: <http://www.geotomosoft.com/downloads.php> (accessed on 15.06.2018).
- Maurer H. and Hauck C. 2007. Geophysical imaging of alpine rock glaciers. *Journal of Glaciology* 53: 110–120. doi: 10.3189/172756507781833893
- Nolet G. 2008. *A breviary of seismic tomography: Imaging the interior of the Earth and Sun*. Cambridge University Press, Cambridge. doi: 10.1017/CBO9780511984709
- Nordli Ø., Wszyński P., Gjeltén H., Isaksen K., Łupikasza E., Niedźwiedz T. and Przybylak R. 2020. Revisiting the extended Svalbard Airport monthly temperature series, and the compiled corresponding daily series 1898–2018. *Polar Research* 39: 1–15. doi: 10.33265/polar.v39.3614
- Nowak A., Hodgkins R., Nikulina A., Osuch M., Wawrzyniak T., Kavan J., Łepkowska E., Majerska M., Romashova K., Vasilevich I., Sobota I. and Rachlewicz G. 2021. From land to fjords: The review of Svalbard hydrology from 1970 to 2019. In: Moreno-Ibáñez M., Hagen J. O., Hübner C., Lihavainen H. and Zaborska A. (eds.) *SESS report 2020. Svalbard Integrated Arctic Earth Observing System, Longyearbyen*: 176–201. doi:10.5281/zenodo.4294063
- Osuch M. and Wawrzyniak T. 2017a. Inter- and intra-annual changes in air temperature and precipitation in western Spitsbergen. *International Journal of Climatology* 37: 3082–3097. doi: 10.1002/joc.4901
- Osuch M. and Wawrzyniak T. 2017b. Variations and changes in snow depth at meteorological stations Barentsburg and Hornsund (Spitsbergen). *Annals of Glaciology* 58(75pt1): 11–20. doi: 10.1017/aog.2017.20
- Owoc B., Marciniak A., Dzierżek J., Kowalczyk S. and Majdański M. 2019. Seismic imaging of the Mesozoic bedrock relief and geological structure under Quaternary sediment cover: The Bolmin Syncline (SW Holy Cross Mountains, Poland). *Geosciences* 9: 447. doi: 10.3390/geosciences9100447
- Pękala K. 1989. Quaternary deposits of the Hans Glacier forefield (Hornsund, Spitsbergen). *Polar Session. Natural Environment Research of West Spitsbergen*, UMCS Lublin: 191–204 (in Polish).
- Revil A. and Glover P.W.J. 1998. Nature of surface electrical conductivity in natural sands, sandstones, and clays. *Geophysical Research Letters* 25: 691–694.
- Rossi G., Accaino F., Boaga J., Petronio L., Romeo R. and Wheeler W. 2017. Seismic survey on an open Pingo system in Adventdalen Valley, Spitsbergen, Svalbard. *Near Surface Geophysics* 16: 89–103. doi: 10.3997/1873-0604.2017037
- Sen P.K. 1968. Estimates of the regression coefficient based on Kendall's tau. *Journal of the American Statistical Association* 63: 1379–1389.
- Senderak K., Kondracka M. and Gądek B. 2021. Processes controlling the development of talus slopes in SW Spitsbergen: The role of deglaciation and periglacial conditions. *Land Degradation & Development* 32: 208–223. doi: 10.1002/ldr.3716
- Sevestre H., Benn D.I., Hulton N.R.J. and Bælum K. 2015. Thermal structure of Svalbard glaciers and implications for thermal switch models of glacier surging. *Journal of Geophysical Research* 120: 2220–2236. doi: 10.1002/2015JF003517
- Wawrzyniak T. and Osuch M. 2020. A 40-year High Arctic climatological dataset of the Polish Polar Station Hornsund (SW Spitsbergen, Svalbard). *Earth System Science Data* 12: 805–815. doi: 10.5194/essd-12-805-2020
- Wawrzyniak T., Osuch M., Napiórkowski J.J. and Westermann S. 2016. Modelling of the thermal regime of permafrost during 1990–2014 in Hornsund, Svalbard. *Polish Polar Research* 37: 219–242. doi: 10.1515/popore-2016-0013

- Van Pelt W., Pohjola V., Pettersson R., Marchenko S., Kohler J., Luks B., Hagen J.O., Schuler T., Dunse T., Noel B. and Reijmer C. 2019. A long-term dataset of climatic mass balance, snow conditions, and runoff in Svalbard (1957–2018). *The Cryosphere* 13: 2259–2280. doi: 10.5194/tc-13-2259-2019
- Zhao W., Forte E., Colucci R.R. and Pipan M. 2016. High-resolution glacier imaging and characterization by means of GPR attribute analysis. *Geophysical Journal International* 206: 1366–1374. doi: 10.1093/gji/ggw208
- Zimmerman R.W. and King M.S. 1986. The effect of the extent of freezing on seismic velocities in unconsolidated permafrost. *Geophysics* 51: 1285–1290. doi: 10.1190/1.1442181

Received 20 December 2021

Accepted 22 April 2022